Article | Received 25 October 2023; Accepted 18 March 2024; Published 12 April 2024
https://doi.org/10.55092/bm20240002

Mimicking 3D bone microenvironment using a hybrid hydrogel-nanocomposite scaffold and human adipose-derived stem cells for bone differentiation and vascularization

Amel Ibrahim[1,2,†,*], Oliver FW Gardner[1], Naira Rodriguez-Florez[1,2,‡], John C Hutchinson[3], Alexander Seifalian[4], Daniel Thomas-Vazque[5], Neil J Sebire[1,3] David Dunaway[1,6], Neil W Bulstrode[1,2], Patrizia Ferretti[1,†,*]

[1] Stem Cells and Regenerative Medicine Section, UCL Great Ormond Street Institute of Child Health, London, UK
[2] Department of Plastic Surgery, Great Ormond Street Hospital for Children NHS Foundation Trust, London, UK
[3] Department of Histopathology, Great Ormond Street Hospital for Children, NHS Foundation Trust, London, UK
[4] Nanotechnology and Regenerative Medicine Commercialization Centre (Ltd), The London Bioscience Innovation Center, London, UK
[5] Johnson Space Center, NASA Pkwy, Houston, Texas, USA
[6] Craniofacial Group-FaceValue UCL Great Ormond Street Institute of Child Health and Great Ormond Street Hospital for Children, London, UK
† Current affiliation: Bioworkshop, New York, USA
‡ Current affiliation: Universidad de Navarra, TECNUN Escuela de Ingenieros, San Sebastian, Spain and IKERBASQUE, Basque Foundation for Science, Bilbao, Spain

* Correspondence authors: Amel Ibrahim and Patrizia Ferretti;
E-mails: amel.ibrahim.11@alumni.ucl.ac.uk; p.ferretti@ucl.ac.uk.

Abstract: Bioengineered bone tissues could bypass limitations of traditional reconstructive methods such as bone grafts or foreign-body implants, but to date this approach has been limited by immaturity of engineered bones and vascularization. Pediatric human adipose-derived stem cells (hADSCs) can be derived using minimally invasive procedures and are known to undergo osteogenic differentiation. Here we have taken a "design-in reverse" approach to tissue engineering by mimicking the native tissue microenvironment to bioengineer complex vascularized tissues. Specifically, we sought to optimize bone tissue engineering by modelling the bone tissue microenvironment and vascularization using hADSCs in combination with a nanocomposite biodegradable nanomaterial and hydrogel, POSS-PCL-fibrin. Our scaffolds exhibited similar architectural features to bone and supported hADSC osteogenic differentiation *in vitro*. Extensive vascularization and formation of tissues resembling pediatric calvarial (upper part of the skull encasing the brain) bone as well as host cell infiltration yielding chimeric tissues were achieved *in vivo* in nude mice. Our results suggest a promising dual tissue engineering purpose for POSS-PCL-fibrin both as a scaffold for bioengineering prefabricated replacement bone tissues and potentially as a bioactive scaffold for *in situ* bone regeneration.

Keywords: Adipose derived stem cells; biomaterial; bone; human; fibrin gel; micro-niche; tissue engineering; vascularization

1. Introduction

Notwithstanding extensive efforts and advances in bone bioengineering, effective treatment of critical size bone deficits caused by either trauma or disease, particularly in children, remains a challenge. This is largely due to the structural complexity and vascularization requirement for bone survival, maturation and homeostasis [1–4]. Crucial to progressing towards a treatment is to create systems that can mimic the physical and structural properties of pediatric bone tissues and support vascularization, survival and differentiation of autologous osteoprogenitor cells. Indeed the ability to bioengineer autologous bone implants would be particularly invaluable in the treatment of pediatric craniofacial deformities where traditional reconstructive procedures are invasive, may provide poor cosmetic outcomes and often require repeated procedures as the child grows [5].

Human adipose derived stem cells (ADSCs) are an attractive source of osteprogenitor cells for bone tissue engineering due to their ease of isolation and availability. They can be derived by minimally invasive procedures from small amounts of pediatric and adult fat, are capable of self-renewal and possess multilineage differentiation potential including osteogenesis [6–13]. Human ADSCs have also been shown to have immune-modulatory properties and promote vascularization, thus making their clinical use attractive [14–16]. Despite this, there remain a number of key barriers to fully harnessing the ADSC osteogenic potential. The most immediate and important consideration is the lack of structural and functional features of mature tissues [17]. To this end, a wide variety of biomaterials have been proposed for bone tissue engineering over the years ranging from hydrogels to bioactive ceramics and polymers.

Hydrogels such as collagen and fibrin have been shown to mimic the extracellular matrix and when decorated with osteoinductive components repair bone defects in rats [18–20].

We and others have previously shown that fibrin is an attractive option for use as a scaffold in human bone tissue engineering as it supports vascularization [17,21]. Fibrin is bioabsorbable, already approved for use in clinical practice and has been shown to promote MSC (mesenchymal stem cell) osteogenesis [17,22]. However, the use of fibrin for bone engineering is curtailed by its limited structural support and mechanical strength. These hydrogels also require extensive and costly modifications to endow them with favorable properties for bone engineering, like increased stiffness, immunomodulation and osteogenic maturation [23,24].

Polymers and bioactive ceramics provide versatile materials to recreate the structural, chemical and mechanical environment needed to support bone tissue regeneration using osteoprogenitor cells *in vitro* and *in vivo* and can be easily and reproducibly manufactured [12,13,17,25–33]. One such versatile nanomaterial is polyhedral oligomeric silsesquioxane (POSS), whose properties vary depending on the groups linked to it, and that can be modified to affect surface, mechanical and architectural properties, and degradability [31,32,34].

Easily customizable and biodegradeable scaffolds can be obtained by using either an aromatic or aliphatic link to attach poly(ϵ-caprolactone-urea) urethane (PCL) to POSS, generating POSS-PCL. The use of a bioabsorbable scaffold that is eventually fully replaced by a well-integrated bone-like tissue would be highly desirable particularly for skeletal reconstruction in pediatric patients where permanent materials may interfere skeletal growth and development.

It has been shown that aromatic forms of POSS-PCL support growth of human MSCs [34] and ADSCs both upon epithelial and chondrogenic differentiation [11]. However, there are known limitations with using nanomaterials like POSS-PCL for bone tissue engineering. Chief amongst them is low bioaffinity which can affect vascularization as well as cell adhesion and although modifications can be made to enhance biocompatibility it still remains a concern for optimizing tissue engineering [35,36].

One emerging approach to create the optimal biological and physiochemical environment for bone tissue engineering is the use of composite scaffolds. These hybrids usually combine two or more biomaterials to augment each other’s properties and overcome their individual limitations. This approach has been used to successfully induce osteogenic differentiation using osteoprogenitor cell laden bioactive hydrogels and synthetic polymers *in vitro* [37] and hydrogel coated polymers *in vivo* [38].

In this study we took a “design- in reverse” approach to tissue engineering and aimed at mimicking the native tissue microenvironment to generate vascularized bone tissues. We hypothesized that the complementary properties of a fibrin hydrogel and POSS-PCL laden with ADSCs could mimic pediatric bone cytoarchitecture and the stem-cell micro-environment hence potentiate cell survival, osteodifferentiation and extensive vascularization.

The choice of fibrin was based on our previous work showing that a fibrin-based 3D microenvironment supported osteogenesis of pediatric ADSCs [17]. As the POSS-PCL aliphatic form is thought to produce less toxic degradation products than the aromatic one [39,40], we focused on the former and further characterized it. First, we compared POSS-PCL architecture to pediatric calvarial bone and show that this nanomaterial displays similar structural features to bone. Then, we assessed osteogenic potential and vascularization of ADSCs in fibrin-POSS-PCL composite scaffolds both *in vitro* and *in vivo* subcutaneous implantation in nude mice. Together, this study demonstrates that the hybrid scaffold we generated is highly biocompatible and, importantly, supports long-term vascularization as shown by the study in mice. Importantly, the scaffold promoted organized bone formation by human and host cells similar histologically and structurally to pediatric calvarial bone controls. This provides proof-of-concept that replicating the native tissue micro-environment can help direct the osteogenic maturation of adipose-derived osteoprogenitor cells.

2. Methods

All chemicals and reagents for both biomaterials and cell culture work were purchased from Merck Life Science UK Limited, Gillingham SP8 4XT, UK (previously Sigma-Aldrich) unless otherwise stated.

2.1. Biomaterial fabrication, modification, sterilization

Porous coagulated 3-dimensional (3D) aliphatic POSS-PCL discs were prepared as previously described [11,34,41] and the Fourier transform infrared (FTIR) spectrograph confirming POSS-PCL content is shown in Figure S1. Briefly, the aliphatic polymer solution was manufactured by combining the dry polycaprolactone polydiol (2000 mwt) and POSS nanocages. The mixture was heated to 135 °C and then cooled at 90 °C to dissolve the POSS nanocages; 4, 4′ methylenebis(cyclohexyl isocyanate) was then added to the polyol blend and reacted, under nitrogen, at 90 °C for 120 minutes with bismuth neodecanoate catalyst. Dry dimethylacetamide (DMAC) was then added slowly to form a solution that was then cooled to 40 °C. A mixture of ethylenediamine and diethylamine in dry DMAC were added to perform chain extension followed by 1-butanol in DMAC to form the POSS-PCL solution. To fabricate porous POSS-PCL scaffolds, sodium bicarbonate particles (80% wet weight) were dispersed and degassed into an (18% w/w) solution of the POSS-PCL polymer in DMAc containing 2% Tween 80 surfactant using a Thinky AER 250 mixer (Intertonics, Kidlington, UK). Porosity was achieved using porogen leaching with sodium bicarbonate particles (80% wet weight) of 105 μm size. Surface modification (“sprinkling”) was then achieved by sieving 105 μm porogens on the seeding surface during the coagulation process. Sheets of POSS-PCL were cut into 2 mm, 5 mm and 1.5 cm discs as required.

Scaffolds were sterilized using either ultraviolet light (“UV”), 70% ethanol (ETOH), autoclaving (“autoclave”) or 10% Decon (“Decon”; Decon laboratories Limited, East Sussex, UK). To autoclave, scaffolds were exposed to saturated steam at 121 °C for 15 min at pressures of 115 kPa then allowed to cool for 24 hours before use at room temperature. For ethanol sterilization, samples were washed in 70% ethanol for 12 hours then rinsed in serial washes of sterile deionized water at room temperature. For UV sterilization, samples sealed sterile glass Petri dishes were placed under a UV trans-illuminator for 12 hours. In the Decon treated group, scaffolds were placed in 10% Decon solution for 24 hours then washed repeatedly in sterile deionized water.

2.2. Human tissue collection and generation of adipose tissue derived stem cells (hADSCs)

Human tissues were collected from consented pediatric patients undergoing surgery at Great Ormond Street Hospital (GOSH) for Children under ethical approval from the Camden and Islington Community Local Research Ethics Committee (London, UK) REC: 09/H0722/28. Bone was collected from routinely discarded skull tissue (calvarial bone) from children with non-syndromic sagittal craniosynostosis undergoing sagittal spring insertion surgery [42]. Bone samples were washed in phosphate buffered saline (PBS; PAA Laboratories Ocoid, Basingstoke, UK) until blood was no longer visible on the surface and fixed in 4% paraformaldehyde (PFA) for structural analysis.

Surplus lipoaspirates (harvested from the abdominal subcutaneous tissue) were from consented patients undergoing lipofilling procedures for reconstruction of craniofacial defects and processed to isolate hADSCs using previously published protocols [7]. Briefly, fat tissue was washed with PBS until visible blood contamination was eliminated and then digested with 0.05% trypsin/1 mM ethylenediaminetetra-acetic acid (EDTA) (Life Technologies, Warrington, UK) on a shaker at 37 °C for one hour. The cell suspension was centrifugated and cell pellets re-suspended in expansion medium (high glucose Dulbecco's modified Eagle's medium (DMEM) containing GlutaMAX and supplemented with 10% embryonic stem cell-qualified fetal bovine serum (ES-FBS) and 1% penicillin/streptomycin (all Life Technologies, Warrington, UK). Cells were grown in expansion medium and passaged when about 70% confluent. Cells were grown and differentiated in a humidified incubator at 37 °C with 5% CO_2.

Osteogenic differentiation was induced by supplementing the expansion medium with 0.1 μM dexamethasone, 100 mM β-glycerophosphate and 100 μg/mL ascorbate-2-phosphate for 3 weeks.

Cell viability under different experimental conditions was assessed by the Resazurin assay (Bio-Rad, Hercules, CA).

2.3. Preparation of cellularized scaffold

To seed POSS-PCL, 10^5 cells per 1.5 cm diameter scaffolds were suspended in expansion medium; half of the cells were seeded onto one side of scaffold and left for 30 minutes in a CO_2 tissue culture incubator at 37 °C. The scaffold was then turned, the remaining cell suspension seeded onto it, and kept for 30 minutes in the incubator before adding expansion media. The following day, scaffolds were transferred to a new plate with fresh medium.

For fibrin scaffold preparation, freshly passaged cells were suspended in sterile bovine thrombin solution (100 iU/mL then combined with 10 mg/ml fibrinogen to obtain 100 μL cellularised fibrin constructs containing 10^5 cells per scaffold. Cellularised scaffolds were allowed to polymerize for 30 minutes in a tissue culture incubator before adding expansion medium. Fibrin was also used as a cell carrier to create hybrid hydrogel/nanocomposite scaffolds (POSS-PCL-fibrin). Fibrin in a volume that was half that of the scaffold was used to seed 10^5 cells onto coagulated POSS-PCL. Cellularised scaffolds were then left to polymerize for 30 minutes before adding expansion medium.

2.4. Fibrin scaffold contraction assay

hADSCs from three separate donors were seeded into fibrin scaffolds made with a final concentration of 16.5 mg/mL fibrinogen (EMD Millipore) and 0.5 U/mL thrombin (EMD Millipore). Scaffolds were cast in agarose molds with a diameter of 8 mm and a total volume of 100 μL. Cells were seeded at a density of $1x10^6$ cells/ml, three technical replicates were made per donor. Once cast the scaffolds were incubated at 37 °C and 5% CO_2 for forty minutes to polymerize, before removal of the agarose mold and release of the scaffolds from the underlying culture plate. Scaffolds were cultured in DMEM (Gibco) supplemented with 5% human platelet lysate (STEMCELL Technologies) and 1% penicillin/streptomycin (Gibco). Immediately after seeding and then again one, two, three, five, six and seven days after seeding the media was removed and the scaffolds were imaged next to a ruler. The surface area of each scaffold was determined from the images using Fiji image analysis software [43]. To do this the scale was set using the ruler present in each image, the polygon tool was then used to draw around each scaffold and the area determined using the measure function.

2.5. In vivo studies

Chick chorioallantoic membrane (CAM) grafting was performed using previously published methods under project license (PPL70-7339) [11]. POSS-PCL scaffolds (n = 6 per condition) were grafted at the site of a bifurcating blood vessel in fertilized brown Leghorn eggs (Needle Farm, UK). Samples were harvested with a cuff of CAM from the egg after anaesthetizing the embryo with 1% chirocaine then fixed in 4% paraformaldehyde (PFA). Chick embryos were sacrificed by decapitation. All CAM experiments were conducted using a minimum of 6 replicates.

Human ADSCs from 3 individual patients were encapsulated in either fibrin alone or seeded onto POSS-PCL-fibrin 5 mm scaffolds and cultured in control or osteogenic differentiation media for three weeks in experimental triplicates then harvested and either analyzed as pre *in vivo* controls, or subcutaneously engrafted onto the flanks of female nude mice (athymic strain CD1/Fcxn-1) using a 1cm incision bilaterally. A total of 6 scaffolds from one donor were engrafted per experimental condition. Animals were checked regularly to ensure wound healing and general welfare. Scaffolds were harvested after 4 months in mice euthanized with carbon dioxide and cervical dislocation. All mouse work was carried out under project license (PPL70/7504) and personal license (I893881EE).

2.6. Histology and immunostaining of cellularised constructs and tissues

For histology, immunocytochemistry or immunohistochemistry, tissues and cells were fixed in 4% PFA. Tissue samples were paraffin-embedded, sectioned (4 µm thickness) and sections stained with Alcian blue/periodic acid Schiff (PAS) or hematoxylin & eosin (H&E) by Great Ormond Street Hospital Histopathology Department. Alcian blue/PAS staining was performed by incubating deparaffinized with 1% alcian blue at pH 2.5 for 30 minutes, followed by a brief incubation in 1% acetic acid, treatment with periodic acid for 5 minutes, and with Schiff's reagent for 15 minutes. Nuclei were counterstained with hematoxylin. For H&E staining, samples were stained with hematoxylin for 4 minutes. This was followed by differentiation with 0.3% acid alcohol before counter staining with eosin.

For immunoflourescent staining, samples were treated with blocking buffer (3% BSA, 10% FBS and 0.2% Triton-X) for 60 minutes prior to incubation with primary antibody overnight at 4 °C then secondary antibody for 1 hour at room temperature. Negative controls where the primary antibody was omitted were run for all conditions (Figure S2). Primary and secondary antibodies used are listed in Table S1.

2.7. Cell, tissue and bioscaffold imaging

Fluorescence imaging of slides and plates was performed using an inverted microscope Olympus IX71 (Zeiss) with a Hamamatsu ORCA-ER digital camera (Hamamatsu Corp) using HCImage processing software. Histological stain images were taken using the Axiovert 135 (Zeiss, Welwyn Garden City, UK) with a ProgRes C14 colour digital camera using Openlab software (PerkinElmer Life, Wokingham, UK).

An upright Zeiss LSM 880 multiphoton was used to image wholemount samples with accompanying Zen software (Zeiss, Welwyn Garden City, UK) and to perform second harmonic generation (SHG) scanning to visualize collagen fibers. All images were processed and interpreted using ImageJ software [44]. To study cellular morphology, nuclei counterstained with Hoechst [11] were segmented then analyzed for circularity as well as area in ImageJ using the ParticleAnalyzer plugin [44]. 181412.581 μm^2 areas were analyzed (at least n = 20 per condition). OrientationJ plugin was used to analyze collagen fiber orientation [45].

Reflection microscopy was performed using the Zeiss multiphoton. ImageJ was used to analyze all data in grey scale 8-bit mode. The plug-in Extended Depth of Field [46] was used to compute a 32-bit height map, and then SurfCharJ plugin [47] to compute surface roughness. To allow comparison between samples, surface levelling, a sample length of 10 µm and a Gaussian filter were applied. Arithmetical mean deviation (Ra) and Root mean square deviation (Rq) were used to quantify surface roughness.

High-resolution µCT scanning was performed using an XTH225 ST microfocus-CT scanner (Nikon Metrology, Tring, United Kingdom) with a multi-metal target set to Molybdenum without X-ray filtration. All scans used an accelerating voltage of 80 kV, a current of 88 µA, exposure time of 500 ms and 3141 projections and one frame per projection. CT scans were reconstructed with the CTPro3D software (version 5.1.1, Nikon Metrology UK) using a modified Feldkamp filtered back projection. The resultant volumes had a voxel size of 12.7 µm equivalent to an approximate resolution of 13 µm. Prior to scanning, samples were fixed in 4% PFA, incubated with iodine for 48 hours, washed and then paraffin embedded. ImageJ was used to post-process 2D stacks of the reconstructed image and analyze them as below.

The WEKA trainable segmentation plugin for ImageJ was used to segment the scaffold, blood vessel and mineralization of the samples [48]. Quantitative analysis of mineralization was performed using the BoneJ plugin [49]. Bone volume fraction (BV/TV) was computed as a ratio of the mineral pixels (BV) and total volume of the scaffold pixels (TV). A particle analyzer plugin was used to measure the area of mineralized nodules and blood vessels. Structural assessment of bone controls and scaffolds was performed using 3D stacks of constant size (236 × 236 pixels) taken from different parts of the center of samples.

2.8. Mechanical testing

Uniaxial compression testing using the Hounsfield tensile and a compression testing machine with a 10 kN Load cell were used to measure deformation and force and derive stress-strain curves. To assess mechanical properties of scaffolds common parameters such as the Young's modulus (E), yield strain (εy), yield stress (σy) and the material's maximum capacity to elastically absorb energy (UelMax) were used. Stress was plotted against strain for each sample to generate a stress-strain profile (Table S2). The point on the curve at which linear elastic behavior ceases was used to determine yield strain and yield stress, which were then used to determine the material's maximum capacity to elastically absorb energy ($UelMax = 1/2\sigma y\varepsilon y$).

2.9. Gene expression analysis by Reverse Transcription Polymerase Chain Reaction (RT- PCR)

RNA was isolated using TRizol (Life Technologies) and reverse transcribed (M-MLV; Promega, Madison, USA) as per manufacturers' protocols. Real time semi-quantitative PCR (RT-qPCR) was performed using primers targeting genes of interest (Table S3) with the ABI Prism 7500 sequence detection system (Applied Biosystems, California, USA) and the Quantitect SYBR Green PCR kit (Qiagen, Hilden, Germany). All samples were run in technical and biological triplicates (n = 3 individual lines per cell type). Data were analyzed using the $\Delta\Delta$CT method.

2.10. Statistical analysis

Unless otherwise stated, experiments were performed in at least 3 experimental replicates, and where hADSCs were used, experiments were performed in biological triplicates using cells from at least 3 individual patients. All data are presented as the mean ± standard error of mean (SEM). Statistical analysis was performed using GraphPad Prism 7.0 for mac (GraphPad software, La Jolla, USA). Statistical significance was evaluated using ANOVA followed by a Tukey's post-hoc test for multiple comparisons. A p-value equal to or less than 0.05 was considered statistically significant.

3. Results

3.1. Characterization of cellularized fibrin

We previously showed that fibrin supports bone tissue engineering by pediatric osteoprogenitor cells and promotes vascularization [17], and fibrin stiffness has been shown to regulate stem cell behavior [50]. Hence, to better understand the physical behavior of fibrin scaffolds during early stages of tissue engineering [50], we analyzed hADSC seeded fibrin gel contraction. The data reveals significant shrinking in gels over the first 7 days of cell culture ($p < 0.05$), that can limit the suitability of fibrin alone for providing mechanical stability at early stages of bone formation (Figure S3).

3.2. Comparison of calvarial bone and porous POSS-PCL scaffolds

We studied the architecture of calvarial bone and POSS-PCL scaffolds using µCT reconstructions of representative samples from the top, middle and bottom of the scanned region (n = 6) (Figure 1(a)). Volumetric representations show both bone and POSS-PCL consist of an inner lattice of solid struts and compact surface layer. Heat maps revealed non-uniform spacing of interconnecting processes. POSS-PCL had greater porosity ($p < 0.05$) and reduced pore size ($p < 0.0001$) (Figure 1(b)). POSS-PCL struts also had smaller "trabecular size" ($p < 0.01$) and 'trabecular density' ($p < 0.01$). Hence, we further investigated its properties following different modifications.

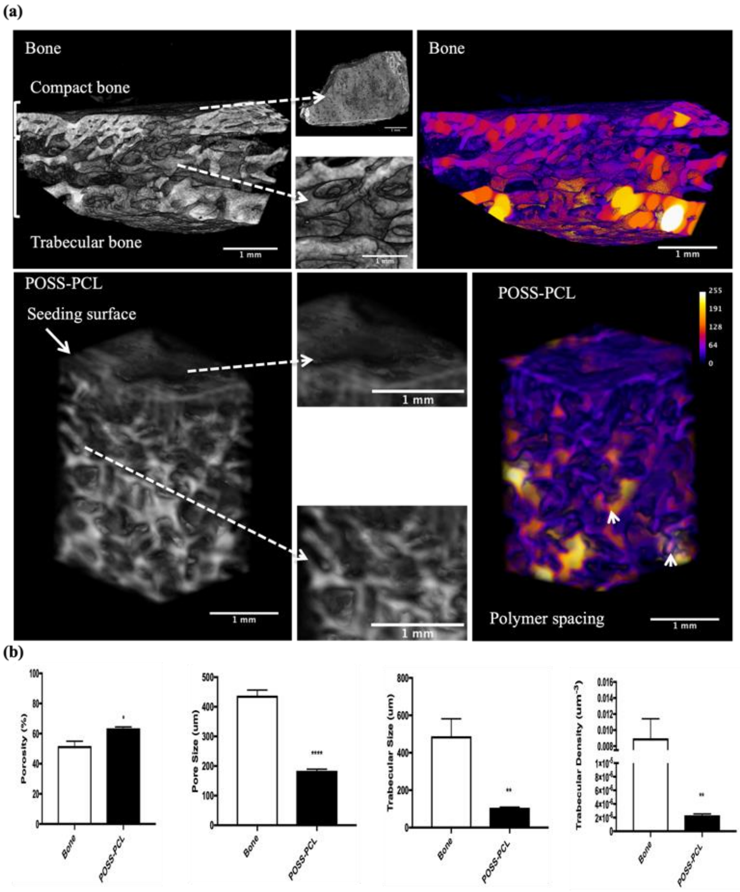

Figure 1. Comparison of porosimetry between 3D POSS-PCL scaffolds and pediatric calvarial bone for tissue engineering by µCT structural analysis. **a)** 3D reconstruction of bone and POSS-PCL µCT images showing a trabecular structure in both. The difference between the compact outer layer of bone and the inner spongy layer (arrows) is replicated by the seeding surface and more porous core of POSS-PCL. Heat maps illustrate the trabecular density and (yellow is thickest) revealing thinner but similarly spaced trabeculae in the scaffold. **b)** Quantitative analysis demonstrates increased porosity and smaller pore size, trabecular size and trabecular density in POSS-PCL (n = 6 samples per group). All data are expressed as mean ± SEM; * $p < 0.05$, ** $p < 0.01$, **** $p < 0.0001$.

3.3. Analysis of POSS-PCL scaffold properties, biocompatibility and vascularization potential

To assess the relevance of changing surface topography on hADSC behavior we created coagulated POSS-PCL scaffolds with rougher topography on the seeding surface ("sprinkled") and compared them with controls ("plain"). Reflected surfaces and corresponding heat maps appear "rougher" on sprinkled samples and although quantitative analysis of roughness was higher in sprinkled (Rq 1.217 ± 0.1603, Ra 0.9500 ± 0.1216) compare with Plain (Rq 1.23 ± 0.1050, Ra 0.9473 ± 0.07668) they did not significantly differ (Figure **2**(a-b)). This may be due to the variability in the sprinkled data which could be due to the non-reproducible manufacturing method. Sprinkled scaffolds had reduced porosity ($p < 0.0001$) and pore size ($p=0.014$) (Figure 2(c)) suggesting the process may disrupt porogen-leaching and alter architecture. Mechanical properties of POSS-PCL were also affected with reduced U_{el}^{Max} ($p < 0.0001$) and yield strength ($p < 0.0001$) in sprinkled scaffolds (Table 1, Figure S4). We assessed whether porosity of these scaffolds would support vascularization after grafting on a CAM ($n = 6$ of each scaffold type) (Figure 2) following optimization of the sterilization protocol (Figure S5). After 7 days on the CAM, both sprinkled and plain scaffolds appeared encased by blood vessels. Hoechst nuclear staining and laminin (LMN) immunolabelling of whole mount samples reveals presence of chick cells on the scaffold and within pores. Positive LMN staining is also seen around the spines of the sprinkled POSS-PCL scaffold and within the pores consistent with vascularization (Figure 2(d)).

Table 1. Effect of altering nanotopography on mechanical strength between plain and modified (sprinkled) POSS-PCL using uniaxial compression testing.

Mechanical Property	**Plain**	**Sprinkled**
E (GPa)	0.94 ± 0.055	0.91 ± 0.02
U_{el}^{Max} (kJ/m^3)	5.51 ± 1.04	0.43 ± 0.30****
Yield strain, σmax (mm/mm)	1.72 ± 0.24	2.23 ± 0.91
Yield stress, εmax (MPa)	6.41 ±0.91	0.47 ± 0.19****

E: Young's modulus; U_{el}^{Max}: compressive strength (maximum capacity to elastically absorb energy).
Statistical significance: *p<0.05; ****p<0.0001.

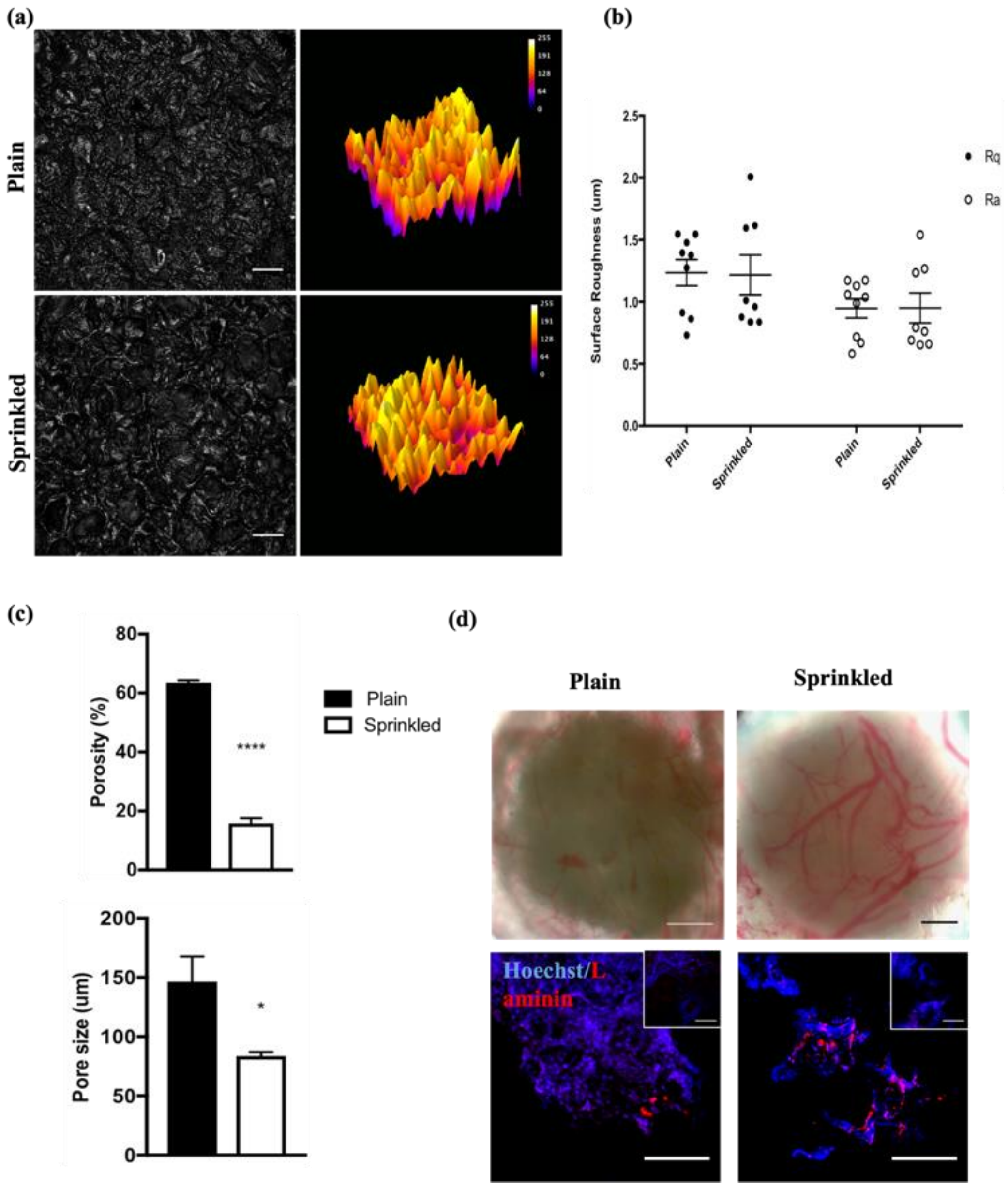

Figure 2. Analysis of the effect of surface modification of coagulated POSS-PCL on topography, structure and vascularization by reflection and immunoflourescent microscopy. **a)** Reflection microscopy of porous POSS-PCL either plain and sprinkled and heat map representations (yellow represents highest pixel and corresponds with increased height) show increased roughness of the sprinkled surfaces. **b)** Quantitative analysis of roughness using Rq and Ra; no significant difference is observed. **c)** Porosity and pore size analyzed by µCT; both are significantly reduced in sprinkled POSS-PCL. **d)** Scaffolds CAM-grafted for 7days. Note more extensive vessel encasement (black arrows) of sprinkled scaffolds (upper panels). Hoechst nuclear staining and laminin expression (lower panels) indicate infiltration of chick cells in both types of scaffolds, but more extensive in sprinkled ones (white arrows). Ra: arithmetical mean deviation; Rq: Root mean square deviation; scale bars=100 µm; statistical significance * $p < 0.05$, **** $p < 0.0001$.

We then assessed whether differences in porosity and pore size affected cell behavior, cellularized scaffolds were cultured in expansion media for 3 weeks. Cells appeared to infiltrate the scaffolds and reside within small pores of both plain and sprinkled POSS-PCL (Figure 3(a)). The hADSCs stained positively for vimentin and cell morphology appeared elongated. There was no significant difference in the morphology or number of cells adhering to the scaffolds but the size of cells on plain POSS-PCL was larger (Figure **3**(b)).

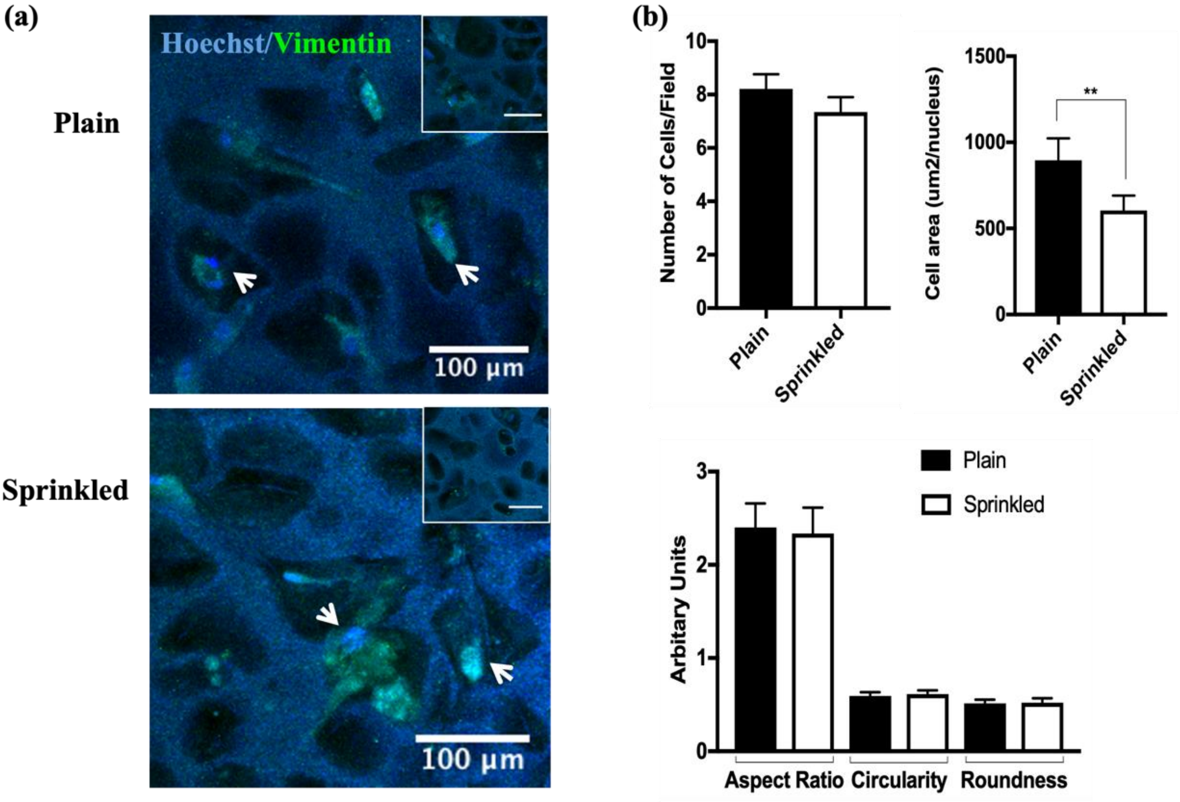

Figure 3. Analysis of the effect of porosity and pore size imparted by surface modification of 3D POSS-PCL on hADSC behavior. **a)** Vimentin positive hADSC populate the pores of the scaffolds (white arrows). **b)** Cells cultured on sprinkled scaffolds are significantly smaller but both scaffolds produce elongated cells (low circularity and roundness). Scale bars=100 µm; statistical significance: ** $p < 0.01$.

These results indicate that whilst sprinkling might better support vascularization, it also reduced strength and in addition the fabrication method was not reproducible. For this reason and given the ability of plain POSS-PCL to support ADSC osteogenic differentiation as indicated by bone protein and gene expression and alizarin red staining (Figures S6 and S7), we chose to use plain coagulated POSS-PCL for further experiments.

3.4. Impact of fibrin-loaded POSS-PCL on vascularization and hADSC osteogenic differentiation

We investigated whether loading POSS-PCL with fibrin would improve vascularization as compared to POSS-PCL (Figure 4). Seven days after CAM-grafting, unseeded POSS-PCL and POSS-PCL-fibrin scaffolds (n = 6) showed encasement and infiltration by blood vessels.

However, fibrin-loaded scaffolds were encapsulated by larger and more numerous blood vessels compared with POSS-PCL alone. Immunoflourescent staining for the blood vessel marker, Von Willebrand Factor (VWF), and Hoechst nuclear staining of whole mounts scaffolds reveal infiltration of chick cells in both scaffolds. Fibrin-loaded scaffolds stained positively for VWF in a pattern consistent with blood vessel lumens.

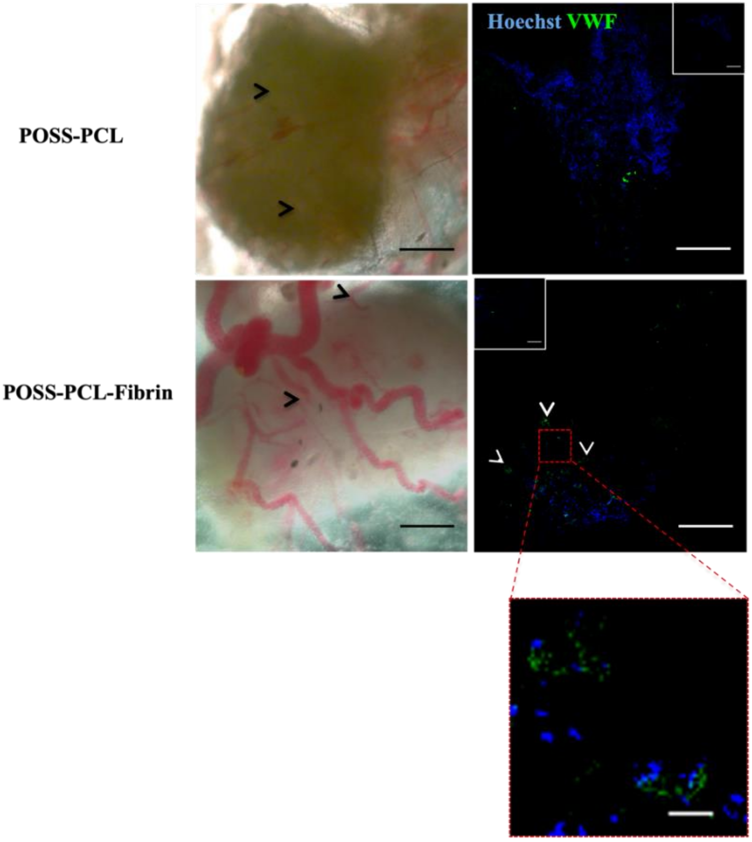

Figure 4. Comparison of vascularization of POSS-PCL alone and POSS-PCL-fibrin composite scaffolds following grafting onto the chick chorioallantoic membrane (CAM). Blood vessels from the CAM surround and infiltrate both types of scaffold. Nuclear staining (Hoechst) within the scaffolds indicates infiltration of chick cells in both scaffold types. VWF (von Willebrand Factor) staining is detected only in the fibrin-containing scaffold. Note VWF luminal distribution (white arrows on main and expanded inset image) consistent with blood.

We then compared hADSC behavior on POSS-PCL and POSS-PCL-fibrin scaffolds after culturing the cellularized scaffold for 3 weeks in control medium. hADSCs were stained for the mesenchymal marker, vimentin, and positive cells were observed on both POSS-PCL and POSS-PCL-fibrin (Figure 5(a)). There was no overall statistically significant difference ($p = 0.26$) in number of adherent cells per field on POSS-PCL (48.94 ± 4.816) versus POSS-PCL-fibrin (55.51 ± 3.186). However, hADSCs appeared widely distributed throughout the POSS-PCL-fibrin scaffold whilst cells on POSS-PCL alone tended to aggregate in patches on the seeding surface and some pores.

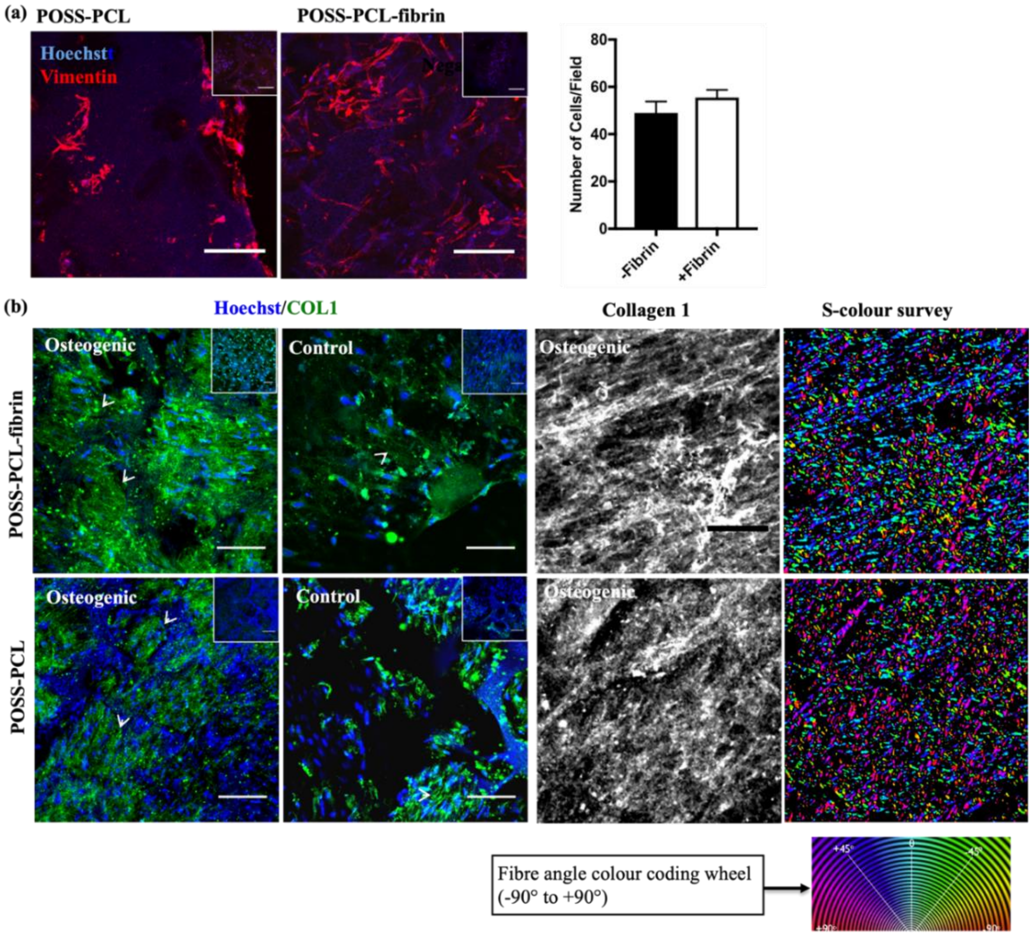

Figure 5. Comparison of hADSC homing and osteogenic differentiation following seeding onto POSS-PCL alone or POSS-PCL-fibrin composite scaffolds by immunoflourescent staining. **a)** Vimentin staining of hADSC cultured on POSS-PCL with and without fibrin; note elongated morphology and difference in cell density between scaffolds. **b)** Collagen type 1 (COL1) immunoflourescent staining and analysis of collagen fibre orientation. Note extensive collagen 1 deposition in both scaffolds (white arrows) upon osteogenic differentiation. Immunolabelled collagen fibre orientation analysis in osteogenic samples is represented as a heat map (S-colour survey with the corresponding colour wheel showing the correlation between colour and orientation. Fibrin-containing scaffolds appear to produce more ordered collagen fibres as evidenced by the orientation, which is mostly between 45 to −45 degrees. Scale bars =100 µm; insets show negative controls with secondary antibody only.

Finally, we compared hADSC osteogenic differentiation in POSS-PCL and POSS-PCL-fibrin scaffolds. COL1 (collagen type 1), a main extracellular matrix (ECM) component in bone, was deposited extracellularly in both scaffolds, but POSS-PCL-fibrin appeared to contain greater fiber density (Figure 5(b)). Moreover, s-colour surveys of collagen fiber orientation and distribution showed relatively high amount of isotropy, which is more akin to ECM organization in native bone. Together, POSS-PCL-fibrin scaffold appears to provide a superior environment for spreading and osteodifferentiation of hADSCs than POSS-PCL alone.

Having previously shown increased ECM deposition and mineralization by hADSCs osteogenically differentiated in fibrin [17], we compared ECM deposition in cellularized fibrin alone and POSS-PCL-fibrin following osteogenic differentiation. Analysis was carried out by double-staining for COL1 and the bone marker OSTP (osteopontin), and SHG (second harmonic generation) scanning to assess collagen fiber orientation (Figure 6). OSTP expression, like COL1, was detected in both scaffolds, but most evident in POSS-PCL-fibrin scaffolds (Figure 6(a)). Fiber orientation from SHG scanning showed collagen fiber networks in osteogenically differentiated cells grown on both. However, there was greater degree of anisotropy of extracellular fibers in fibrin whereas those in POSS-PCL-fibrin were more organized (Figure 6(b-c)).

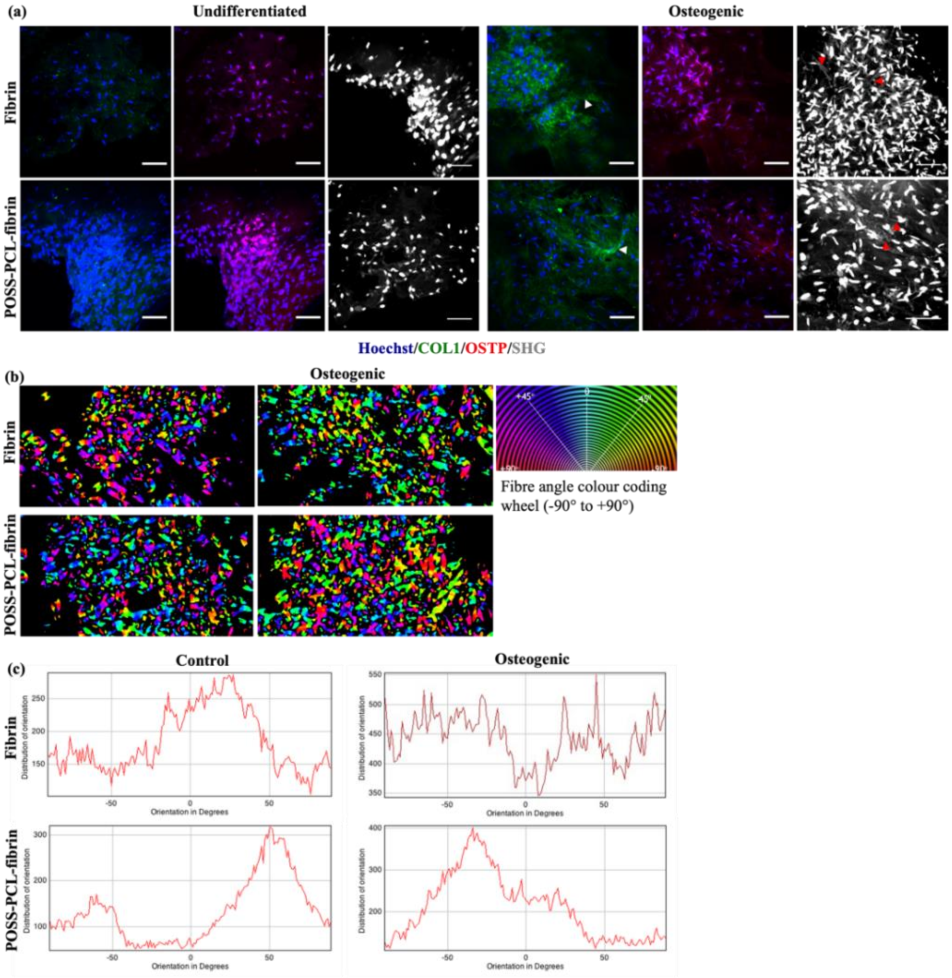

Figure 6. Analysis of ECM formed by hADSC on fibrin and POSS-PCL-fibrin by immunoflourescent staining and second harmonic generation (SHG) scanning. **a)** Immunostaining for COL1 and OSTP and SHG images from osteogenically differentiated scaffolds. Note extracellular COL1 staining (white arrowheads) and limited OSTP expression in control and osteogenic samples. SHG shows collagen fibers (red arrows) on all osteogenically differentiated scaffolds. **b-c)** Collagen fiber orientation analysis after osteogenic differentiation; SHG shows more polarized orientation on POSS-PCL-Fibrin. COL1: collagen 1; OSTP: osteopontin; scale bars: 100 μm.

3.5. *Analysis of hADSC fibrin and POSS-PCL-fibrin following implantation in nude mice*

Cellularized fibrin and POSS-PCL-fibrin scaffolds were grafted subcutaneously in nude mice and retrieved after 4 months with overlying skin, subcutaneous tissue and underlying membrane and compared (Figure 7). Macroscopic images show encasement and vessel growth on scaffold surfaces. H&E staining shows soft tissue growth in and around the scaffolds without obvious inflammation or fibrosis (Figure 7(a)) which can still occur in nude mice which despite their athymic status can still mount non T-cell mediated and innate immune response including granuloma formation [51]. Blood vessels are visible within murine tissues and scaffolds. Periodic acid Schiff (PAS) and alcian blue (AB) staining were used to analyze ECM composition. There was predominance of acid-complex (PAS-/AB+) and acid simple (PAS+/AB+) mucins consistent with skeletogenic and stromal tissues. Osteoblast, osteocyte and osteoclast-like cells were identified in H&E staining of both scaffolds.

Histomorphometric analysis of H&E staining from each scaffold type (n = 3 scaffolds per condition, n = 3 sections per scaffold) showed cellular constituents similar in appearance and localization to bone (Figure 7(a)). Differentiating cellularized scaffolds prior to implantation did not affect osteoblast density in fibrin but increased it in POSS-PCL-fibrin when compared with control POSS-PCL-fibrin ($p = 0.0003$) and fibrin ($p = 0.0002$). Osteocyte and osteoclast numbers were significantly increased in differentiated fibrin and even more in POSS-PCL-fibrin (Table 2).

Table 2. Density of osteoblasts, osteocytes and osteoclasts in different ADSC cellularized scaffolds 4 months after subcutaneous implantation in nude mice.

		Osteoblasts (cells/mm^2)	**Osteocytes (cells/mm^2)**	**Osteoclasts (cells/mm^2)**
Fibrin	Control§	138.22 ± 22.92	48.22 ± 6.26$^{a, c}$ *	2.22 ± 0.52^{b***}
	Osteogenic^	225.44 ± 24.05	105.22 ± 13. 04$^{d\ ***}$	5.44 ± 0.82^{a}*
POSS-PCL-fibrin	Control	120.50 ± 32.10	44.50 ± 2.41	3.71 ± 0.68
	Osteogenic	309.22 ± 27.54$^{a, b}$ ***	188.11 ± 18.70$^{a, b\ ****}$	7.75 ± 1.28^{a}*

§ scaffolds cultured in control medium or ^ in osteogenic medium for 3 weeks prior to subcutaneous implantation. *$p<0.05$, ***$p<0.001$, ****$p<0.0001$.

Pediatric calvarial bone composition was assessed to provide a histomorphometry reference for scaffold analysis (Figure S8(a-c)). Morphology of the main bone cellular constituents (osteoblasts, osteoclasts and osteocytes) was defined using well established criteria [52]. Areas between 537.6-9593.3 μm^2 were selected in sections of bone from individual patients (n = 7) for quantitative analysis (Figure S8(d)). Average cell density of 2.82 (±0.25) cells per 100μm^2 was found in bone with osteoblasts, osteocytes and osteoclasts comprising 56%, 41% and 3% of total cell density respectively.

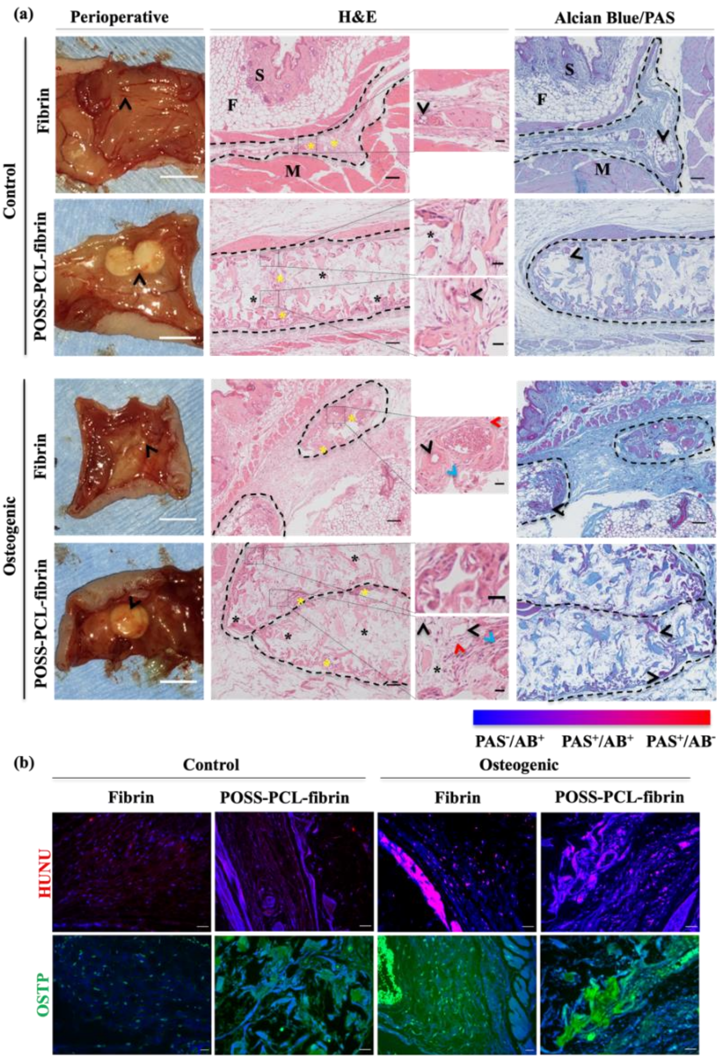

Figure 7. Gross morphology of control and osteogenically differentiated ADSC fibrin and POSS-PCL-fibrin scaffolds and analysis of scaffold sections. **a)** Perioperative macroscopic images constructs; note that vessels surround the scaffolds (black arrowheads). H&E (hematoxylin and eosin) staining: note integration of cellularized scaffolds (enclosed by black lines) and stromal/soft tissue growth (yellow asterix); some POSS-PCL-fibrin pores remain acellular (black asterix). Blood vessels (black arrowhead), osteocytes (red arrowhead) and osteoblasts (blue arrow) are identifiable. PAS/AB (periodic acid Schiff/Alcian Blue) staining: proteoglycans are detected within scaffolds and angiogenesis (black arrowhead) with predominance of acid-complex connective tissue mucins (PAS-/AB+) and acid simple mucins (PAS+/AB+). **b)** Detection of the human nuclear antigen, HUNU (red) by immunofluorescence; nuclei are counterstained with Hoechst dye (blue): note presence of HUNU-positive nuclei; HUNU-negative nuclei within the scaffolds indicate infiltration of murine cells. OSTP (osteopontin, green) expression is observed in cells within all scaffolds and differentiation conditions. Scale bars (a) = 5 mm (perioperative)/100 µm (large windows)/25 µm (small windows). Scale bars (b) = 100 µm. F; fat (mouse), M; muscle (mouse), S; skin (mouse).

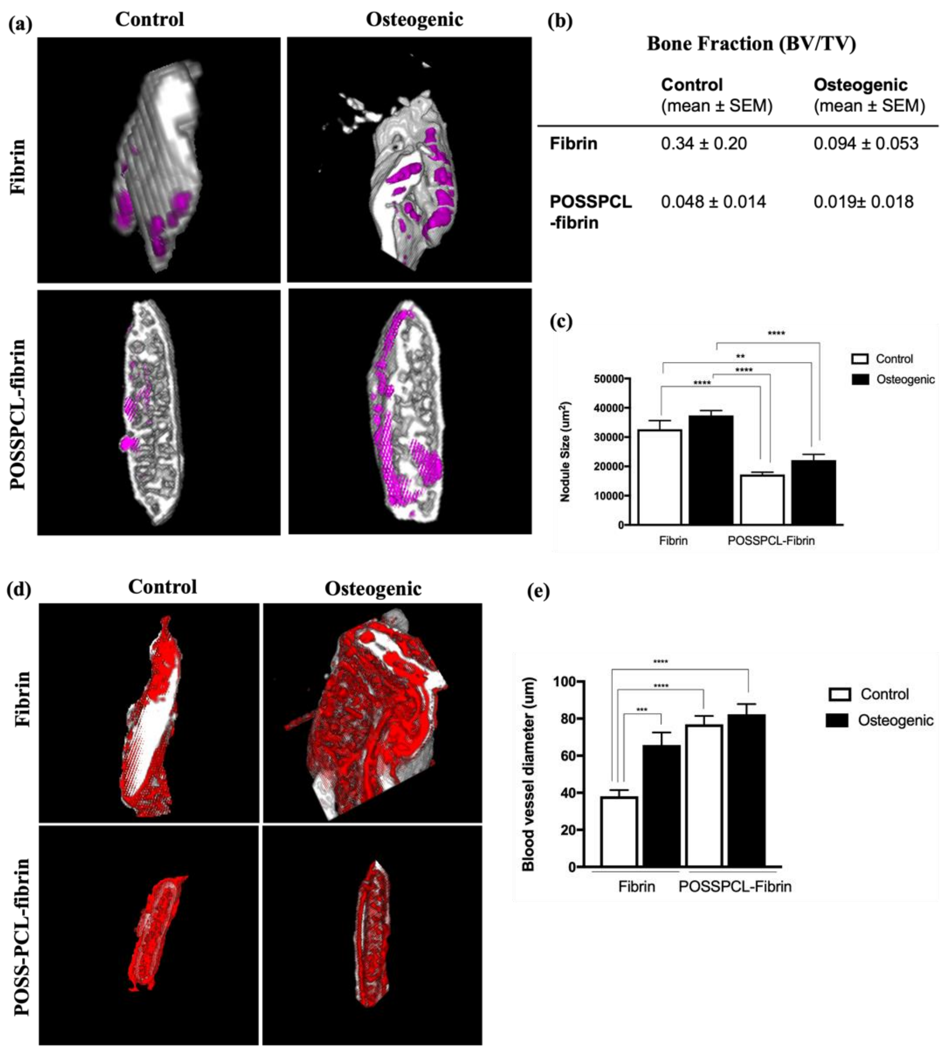

Bone Fraction (BV/TV)

	Control (mean ± SEM)	Osteogenic (mean ± SEM)
Fibrin	0.34 ± 0.20	0.094 ± 0.053
POSSPCL -fibrin	0.048 ± 0.014	0.019± 0.018

Figure 8. μCT analysis of mineralization and vascularization in hADSC-cellularized scaffolds after 4 months subcutaneous implantation in nude mice. **a)** 3D models of segmented scaffolds; note calcium nodule formation (magenta) in undifferentiated control and osteogenically differentiated cellularized scaffolds after 4 months implantation *in vivo*. **b)** Analysis of bone volume fraction in different scaffolds and culture differentiation conditions; no significant difference is observed between groups. **c)** Measurements of bone nodule size: note larger nodules of hADSCs grown on fibrin than POSS-PCL-fibrin; nodule sizes in control and osteogenically differentiated cells grown on the same scaffold type are not significantly different. **d)** 3D models of segmented μCT reconstructed scans: show blood vessels (red) surrounding each scaffold and growing into them (grey). **e)** Analysis of blood vessel diameter: vessel diameter is larger in fibrin scaffolds chondrogenically differentiated prior to implantation, and in control POSS-PCL-fibrin as compared to controls in fibrin alone. There is no significant difference in size of vessels between control and differentiated POSS-PCL-fibrin scaffolds. SEM; standard error of mean; ** $p < 0.01$, *** $p < 0.001$, **** $p < 0.0001$.

Human nuclear antigen (HUNU) and OSTP staining were used to confirm that cells present within the scaffolds were of human origin and contributed to bone tissue (Figure 7(b)). HUNU/Hoechst co-localization was seen within all cellularized scaffolds indicating survival of hADSCs. Presence of HUNU-negative nuclei suggests infiltration of mouse cells and their contribution to bone formation. OSTP was detected in both groups although there appeared to be more OSTP-expressing cells in differentiated implants. We also detected HUNU-positive cells in blood vessels suggesting that undifferentiated hADSC had migrated into surrounding mouse tissues and differentiated into endothelial cells or pericytes as previously reported [53].

Segmented µCT reconstructions were rendered to build 3D models of mineralization and vascularization (Figure 8). Mineralization was detected in undifferentiated control and osteogenically differentiated fibrin and POSS-PCL-fibrin scaffolds; analysis of the bone volume fraction shows no significant differences in mineral density between groups (Figure 8(a-b)). Calcium nodule size was however larger in fibrin than in POSS-PCL-fibrin in both undifferentiated control ($p < 0.0001$) and differentiated scaffolds ($p < 0.0001$). There was no significant difference in bone nodule size between cells cultured in control or osteogenic media grown on the same scaffold type (Figure 8(c)). There was a vascular network surrounding each scaffold regardless of pre-implantation culture condition and evidence of infiltration and ingrowth of blood vessels into POSS-PCL-fibrin (Figure 8(d)). Vessel diameter analysis shows the smallest vessels were found in control fibrin compared with differentiated cells on fibrin ($p < 0.0004$), control cells on POSS-PCL-fibrin ($p < 0.0001$) and differentiated cells on POSS-PCL-fibrin ($p < 0.0001$) (Figure 8(e)). Vessel size did not significantly differ between differentiated cellularized fibrin and control or differentiated cellularized POSS-PCL-fibrin.

4. Discussion

We used a “design-in-reverse” approach to recreate the vascular and physical microenvironment for pediatric bone tissue engineering by hADSC using a hybrid bioabsorbable material that also supports host cell infiltration *in vivo*. To achieve this, we used fibrin as a cell carrier to leverage its abilities to promote cell adhesion, osteogenesis and vascularization. In parallel we modified aliphatic POSS-PCL to model the physical and mechanical bone microenvironment thereby improving its ability to support pediatric hADSC survival and differentiation. Our hybrid POSS-PCL-fibrin when cellularized with hADSCs yielded tissues with similar cellular composition to bone after *in vivo* implantation.

4.1. Structural properties of POSS-PCL recreate bone microenvironment

The cellular microenvironment is known to play a crucial role in directing and regulating cell proliferation and differentiation [54,55]. This is dependent on cell type and warrants a pivot towards recreating specific cell and tissue niches [56,57]. For bone, the 3D microenvironment is vital for osteogenic differentiation and ECM deposition [58,59]. Whilst fibrin scaffolds support vascularization and have shown promise in driving hADSC early osteogenic differentiation, hADSC/fibrin constructs do not maintain their shape overtime, as shown by our gel contraction study, limiting its use alone for bone tissue engineering [60,61]. In contrast, the POSS-PCL scaffolds used here better approximate the extracellular bone microenvironment. They are highly porous with similar structural features to bone. Although porosity was higher and trabecular/biomaterial density was lower, presence of these features still facilitated culture in a bone-like 3D physical environment where we know that porosimetry is an important determinant of cell behavior, mineralization and vascularization [62–64]. Furthermore, scaffold architecture has been shown to affect mouse osteoblast and rat MSC migration, adhesion and mineralization through regulating cell surface integrin and ECM interactions [65]. We also showed that surface modification of POSS-PCL affected hADSC size and increased vascularization. This is in keeping with previous studies showing surface topography influences MSC biology [66–69] and that nanotechnology can be used to mimic biophysical properties of bone ECM to direct differentiation [70,71]. Whilst sprinkled POSS-PCL enhanced vascularization, there was a trade-off in strength and reproducibility.

4.2. Fibrin loading POSS-PCL further enhances vascularization and hADSC osteogenesis

We show here that a hybrid of fibrin-POSS-PCL can overcome each material's individual limitations. POSS-PCL-fibrin retained cellular adhesion and differentiation benefits of POSS-PCL and imparted angiogenic properties that were better than sprinkling. POSS-PCL-fibrin enabled hADSCs to secrete and deposit ECM containing organized collagen fibers as expected in bone. This provides further evidence that the physiochemical environment directs MSC behavior and supports the rationale for engineering a biomimetic scaffold emulating the cellular niches in target tissues. The importance of the physical environment on influencing MSC behavior and osteoinduction was previously shown by using multi-walled carbon nanotube scaffolds which enhanced hADSC mineralization *in vitro* and ectopic bone formation *in vivo* by enabling cell and protein adhesion and interactions similar to those found in bone ECM [72]. Previous work has also shown that deposition of isotropic collagen fiber networks by sheep MSC directed pattern and size of mineral particles resulting in reorganization of collagen fibers [73]. This heterogeneous distribution was not observed in cellularized POSS-PCL-fibrin scaffolds possibly indicating an earlier degree of maturation.

4.3. In vivo implantation of cellularized POSS-PCL-fibrin promotes osteogenic maturation as well as infiltration and vascularization by host cells

Vascularization is integral to bone development, survival and function [74,75]. Cellularized POSS-PCL-fibrin implanted *in vivo* showed biocompatibility and integration. The implants also enabled angiogenesis and ECM deposition independent of pre-differentiation *in vitro*. The impact of early vascularization on promoting osteogenic differentiation and maturation by pediatric hADSC and other osteoprogenitors on fibrin was previously described by us [17]. Other studies have shown that oxygen deprivation impairs matrix maturation of preosteoblast cells *in vitro* [76]. Furthermore induction of hypoxia inducible factor-1α under normoxic conditions promoted angiogenesis and osteogenesis in rat BMSC *in vitro* [77] whilst increasing vascularization and mineralization of critical sized calvarial defects in rats [78,79].

Crucially, POSS-PCL-fibrin contained hADSC after 4 months and evidence of non-human cells *in vivo* in keeping with previous studies that showed chimerized tissue formation when cellularized scaffolds were implanted in mice [80]. The diameter of the vessels infiltrating the scaffolds suggests microvasculature formation. Previously, mapping of vasculature in murine calvarial bone marrow has shown that flow dynamics in these vessels directed haemopoietic and progenitor cell homing [81]. Our implanted constructs also formed a structure resembling mature skeletogenic connective tissue. This is in-keeping with studies that mimicked the complex arrangement of osteoprogenitor cells and blood supply in bone by co-culture of human MSC and umbilical vein endothelial cells to bioengineer vascularized functional bone subunits *in vitro* [82]. Recreating bone blood supply by prevascularisation of tissue engineered bone grafts using a bioceramic scaffold and MSC with femoral blood vessels was also shown to enhance bone regeneration and angiogenesis in rabbit fractures [83].

In addition to vascularization by host vessels, there was also evidence of infiltration of the scaffolds by mouse cells alongside hADSCs which were still present after 4 months *in vivo*. Although cellularity was not high, cells within the scaffolds resembled osteoblasts, osteocytes and osteoclasts consistent with establishment of a microenvironment similar to bone. Ability of the scaffold to both support hADSC seeded prior to implantation and attract host cells has important implications for POSS-PCL-fibrin in bone bioengineering. Presence of host cells potentially provides an additional use-case for POSS-PCL-fibrin as an implant for bone regeneration by promoting host cell colonization. This is in keeping with current trends in tissue engineering that use biomaterials to facilitate autologous tissue engineering *in vivo*. The use of bioceramic, alloy and nanomaterial implants to promote bone regeneration using the *in vivo* environment as a bioincubator has already shown promise in animal fracture repair models [84,85].

POSS-PCL-fibrin's ability to accommodate both *in situ* and *in vitro* bioengineering provides greater flexibility in its potential for creating both prefabricated bioengineered bone replacement tissues and bioactive implants. Whilst mineralization density was not affected by osteogenic differentiation prior to *in vivo* implantation, presence of bone related cells and an organized ECM was significantly enhanced by osteogenic priming of the cellularized scaffolds prior to implantation, which is indicative of more advanced bone maturation. This supports previous studies which have shown that osteogenic differentiation of human osteprogenitor cells can be enhanced by culture on scaffolds that mimic ECM patterning [59] and even more so when combined with physical stimulation to reproduce the bone biomechanical environment [86]. Our findings are in-keeping with increasing recognition of the concept of the bone organ as defined by vasculature, the presence of an organic and inorganic ECM and interplay between the osteogenic cells as key to establishing the basis for bioengineering [87–89].

5. Conclusion

This study sought to model the bone-specific tissue microenvironment to drive bone tissue engineering by hADSC. We fabricated a novel hybrid fibrin-nanocomposite scaffold, POSS-PCL-fibrin, that utilizes the properties of hydrogels and synthetic polymers to support hADSC survival, differentiation and vascularization *in vitro* and *in vivo*. Our findings provide important considerations for bioengineering replacement bone tissues using pediatric hADSC whose maturation can be further enhanced *in vivo*. The ability for host cell infiltration on this resorbable biomaterial also hint at promise of POSS-PCL-fibrin as a standalone implant for *in situ* bone regeneration.

Supplementary data

The authors confirm that the supplementary data are available within this article.

Acknowledgment

This work was supported by the RCS Blond Research Training Fellowship, The RCS Fulbright Scholarship, Newlife Foundation, Great Ormond Street Hospital Children's Charity and GOSH NIHR Biomedical Research Centre. We are most grateful to Dr Dale Moulding at the ICH Microscopy Facility for his advice on acquisition and analysis of the results. We also wish to thank our colleagues Arnold Darbyshire, Peter Butler, Leonardo Guasti, N.U. Owase Jeelani, Silvia Schievano and Deborah Eastwood for helpful discussions and mentorship.

Conflicts of interests

The authors declare no conflict of interest.

Ethical statement

The study involving human samples was performed in accordance with the Declaration of Helsinki and approved by the Camden and Islington Community Local Research Ethics Committee (London, UK) REC: 09/H0722/28 (August 2018).

The study involving animal experiments, was performed under project license PPL70-7339 (chick work) and PPL70/7504 (mouse work) approved by the UK Home Office (initially in August 2011 and regularly renewed).

Authors' Contribution

AI designed and performed experiments, analyzed data, wrote the manuscript and obtained funding; NRF, OFWG, JCH, DTV and NJS contributed to histology, μCT analysis and mechanical testing and provided critical reading of manuscript; NRF, NWB and DD obtained patient consent, collected tissues and provided critical reading of manuscript; AS contributed to scaffold design and fabrication and provided critical reading of manuscript; PF supervised research, analyzed data, obtained funding, and edited manuscript.

References

[1] Sims NA, Martin TJ. Coupling the activities of bone formation and resorption: a multitude of signals within the basic multicellular unit. *Bonekey Rep.* 2014, 3:481.

[2] Lafage-Proust MH, Roche B, Langer M, Cleret D, Vanden Bossche A, *et al.* Assessment of bone vascularization and its role in bone remodeling. *Bonekey Rep.* 2015, 4:662.

[3] Boerckel JD, Uhrig BA, Willett NJ, Huebsch N , Guldberg RE. Mechanical regulation of vascular growth and tissue regeneration *in vivo*. *Proc Natl Acad Sci U S A.* 2011, 108(37):E674–680.

[4] Vogt MT, Cauley JA, Kuller LH , Nevitt MC. Bone mineral density and blood flow to the lower extremities: the study of osteoporotic fractures. *J Bone Miner Res.* 1997, 12(2):283–289.

[5] Capitelli-McMahon H, Kahlar N , Rahman S. Titanium Versus Autologous Bone-Based Cranioplasty: A Systematic Review and Meta-Analysis. *Cureus.* 2023, 15(5):e39516.

[6] Levi B, Longaker MT. Concise review: adipose-derived stromal cells for skeletal regenerative medicine. *Stem Cells.* 2011, 29(4):576–582.

[7] Guasti L, Prasongchean W, Kleftouris G, Mukherjee S, Thrasher A, *et al.* High plasticity of paediatric adipose tissue-derived stem cells: too much for selective skeletogenic differentiation? *Stem Cells Transl Med.* 2012, 1(5):384–395.

[8] Zuk PA, Zhu M, Ashjian P, De Ugarte DA, Huang JI, *et al.* Human adipose tissue is a source of multipotent stem cells. *Mol Biol Cell.* 2002, 13(12):4279–4295.

[9] Philips BJ, Marra KG , Rubin JP. Adipose stem cell-based soft tissue regeneration. *Expert Opin Biol Ther.* 2012, 12(2):155–163.

[10] Planat-Benard V, Silvestre JS, Cousin B, André M, Nibbelink M, *et al.* Plasticity of human adipose lineage cells toward endothelial cells: physiological and therapeutic perspectives. *Circulation*. 2004, 109(5):656–663.

[11] New SEP, Ibrahim A, Guasti L, Zucchelli E, Birchall M, *et al.* Towards reconstruction of epithelialized cartilages from autologous adipose tissue-derived stem cells. *J Tissue Eng Regen Med.* 2017, 11(11):3078–3089.

[12] Herrera D, Lodoso-Torrecilla I, Ginebra MP, Rappe K , Franch J. Osteogenic differentiation of adipose-derived canine mesenchymal stem cells seeded in porous calcium-phosphate scaffolds. *Front Vet Sci.* 2023, 10:1149413.

[13] Wang D, Wang H, Yan Y, Wei N, Jaspers RT, *et al.* Coating 3D-Printed Bioceramics with Histatin Promotes Adhesion and Osteogenesis of Stem Cells. *Tissue Eng Part C Methods.* 2023, 29(7):321–331.

[14] Jeon S, Kim I, Na YR, Yong Hong K, Chang H, *et al.* Multiple Injections of Adipose-Derived Stem Cells Improve Graft Survival in Human-to-Rat Skin Xenotransplantation through Immune Modulation. *Tissue Eng Regen Med.* 2023, 20(6):905–919.

[15] Gao S, Calcagni M, Welti M, Hemmi S, Hild N, *et al.* Proliferation of ASC-derived endothelial cells in a 3D electrospun mesh: impact of bone-biomimetic nanocomposite and co-culture with ASC-derived osteoblasts. *Injury*. 2014, 45(6):974–980.

[16] Peng W, Gao T, Yang ZL, Zhang SC, Ren ML, *et al.* Adipose-derived stem cells induced dendritic cells undergo tolerance and inhibit Th1 polarization. *Cell Immunol.* 2012, 278(1-2):152–157.

[17] Ibrahim A, Rodriguez-Florez N, Gardner OFW, Zucchelli E, New SEP, *et al.* Three-dimensional environment and vascularization induce osteogenic maturation of human adipose-derived stem cells comparable to that of bone-derived progenitors. *Stem Cells Transl Med.* 2020, 9(12):1651–1666.

[18] Machado EG, Issa JP, Figueiredo FA, Santos GR, Galdeano EA, *et al.* A new heterologous fibrin sealant as scaffold to recombinant human bone morphogenetic protein-2 (rhBMP-2) and natural latex proteins for the repair of tibial bone defects. *Acta Histochem.* 2015, 117(3):288–296.

[19] Quinlan E, Thompson EM, Matsiko A, O'Brien FJ , López-Noriega A. Long-term controlled delivery of rhBMP-2 from collagen-hydroxyapatite scaffolds for superior bone tissue regeneration. *J Control Release.* 2015, 207:112–119.

[20] Wu P, Shen L, Liu HF, Zou XH, Zhao J, *et al.* The marriage of immunomodulatory, angiogenic, and osteogenic capabilities in a piezoelectric hydrogel tissue engineering scaffold for military medicine. *Mil Med Res.* 2023, 10(1):35.

[21] Noori A, Ashrafi SJ, Vaez-Ghaemi R, Hatamian-Zaremi A , Webster TJ. A review of fibrin and fibrin composites for bone tissue engineering. *Int J Nanomedicine.* 2017, 12:4937–4961.

[22] Lohse N, Schulz J , Schliephake H. Effect of fibrin on osteogenic differentiation and VEGF expression of bone marrow stromal cells in mineralised scaffolds: a three-dimensional analysis. *Eur Cell Mater.* 2012, 23:413–424.

[23] Gao Y, Zhang X , Zhou H. Biomimetic Hydrogel Applications and Challenges in Bone, Cartilage, and Nerve Repair. *Pharmaceutics.* 2023, 15(10).

[24] Zhang J, Tong D, Song H, Ruan R, Sun Y, *et al.* Osteoimmunity-Regulating Biomimetically Hierarchical Scaffold for Augmented Bone Regeneration. *Adv Mater.* 2022, 34(36):e2202044.

[25] Rossi F, Santoro M , Perale G. Polymeric scaffolds as stem cell carriers in bone repair. *J Tissue Eng Regen Med*. 2013.

[26] Lan L, Zhang Q, Zhang H, Yang X, Li S, *et al.* Preparation of hydroxyapatite coated porous carbon nanofibres for DEX loading and enhancing differentiation of BMSCs. *RSC Adv*. 2023, 13(44):30898–30904.

[27] Baino F, Novajra G, Vitale-Brovarone C. Bioceramics and Scaffolds: A Winning Combination for Tissue Engineering. *Front Bioeng Biotechnol*. 2015, 3:202.

[28] Nii M, Lai JH, Keeney M, Han LH, Behn A, *et al.* The effects of interactive mechanical and biochemical niche signaling on osteogenic differentiation of adipose-derived stem cells using combinatorial hydrogels. *Acta Biomater.* 2013, 9(3):5475–5483.

[29] Minardi S, Corradetti B, Taraballi F, Sandri M, Van Eps J, *et al.* Evaluation of the osteoinductive potential of a bio-inspired scaffold mimicking the osteogenic niche for bone augmentation. *Biomaterials.* 2015, 62:128–137.

[30] Safari B, Aghazadeh M , Aghanejad A. Osteogenic differentiation of human adipose-derived mesenchymal stem cells in a bisphosphonate-functionalized polycaprolactone/gelatin scaffold. *Int J Biol Macromol.* 2023, 241:124573.

[31] Griffin MF, Ibrahim A, Seifalian AM, Butler PEM, Kalaskar DM, *et al.* Argon plasma modification promotes adipose derived stem cells osteogenic and chondrogenic differentiation on nanocomposite polyurethane scaffolds; implications for skeletal tissue engineering. *Mater Sci Eng C Mater Biol Appl.* 2019, 105:110085.

[32] Griffin MF, Ibrahim A, Seifalian AM, Butler PE, Kalaskar DM, *et al.* Chemical group-dependent plasma polymerisation preferentially directs adipose stem cell differentiation towards osteogenic or chondrogenic lineages. *Acta Biomater.* 2017, 50:450–461.

[33] Gao C, Deng Y, Feng P, Mao Z, Li P, *et al.* Current progress in bioactive ceramic scaffolds for bone repair and regeneration. *Int J Mol Sci.* 2014, 15(3):4714–4732.

[34] Chawla R, Tan A, Ahmed M, Crowley C, Moiemen NS, *et al.* A polyhedral oligomeric silsesquioxane-based bilayered dermal scaffold seeded with adipose tissue-derived stem cells: in vitro assessment of biomechanical properties. *J Surg Res.* 2014, 188(2):361–372.

[35] Sowmya B, Hemavathi AB, Panda PK. Poly (epsilon-caprolactone)-based electrospun nano-featured substrate for tissue engineering applications: a review. *Prog Biomater.* 2021, 10(2):91–117.

[36] Bagheri L, Valizadeh H, Dindar-Safa K, Zarghami N. Fabricating a robust POSS-PCL nanofiber scaffold for nesting of mesenchymal stem cells: potential application in bone tissue regeneration. *J Biol Eng.* 2022, 16(1):35.

[37] Chen YT, Chuang YH, Chen CM, Wang JY, Wang J. Development of hybrid scaffolds with biodegradable polymer composites and bioactive hydrogels for bone tissue engineering. *Biomater Adv.* 2023, 153:213562.

[38] Lin S, Maekawa H, Moeinzadeh S, Lui E, Alizadeh HV, *et al.* An osteoinductive and biodegradable intramedullary implant accelerates bone healing and mitigates complications of bone transport in male rats. *Nat Commun.* 2023, 14(1):4455.

[39] Wendels S, Avérous L. Biobased polyurethanes for biomedical applications. *Bioact Mater.* 2021, 6(4):1083–1106.

[40] Tang YW, Labow RS , Santerre JP. Isolation of methylene dianiline and aqueous-soluble biodegradation products from polycarbonate-polyurethanes. *Biomaterials.* 2003, 24(17):2805–2819.

[41] Raghunath J, Georgiou G, Armitage D, Nazhat SN, Sales KM, *et al.* Degradation studies on biodegradable nanocomposite based on polycaprolactone/polycarbonate (80:20%) polyhedral oligomeric silsesquioxane. *J Biomed Mater Res A.* 2009, 91(3):834–844.

[42] Rodriguez-Florez N, Ibrahim A, Hutchinson JC, Borghi A, James G, *et al.* Cranial bone structure in children with sagittal craniosynostosis: Relationship with surgical outcomes. *J Plast Reconstr Aesthet Surg.* 2017, 70(11):1589–1597.

[43] Schindelin J, Arganda-Carreras I, Frise E, Kaynig V, Longair M, *et al.* Fiji: an open-source platform for biological-image analysis. *Nat Methods.* 2012, 9(7):676–682.

[44] Schneider CA, Rasband WS , Eliceiri KW. NIH Image to ImageJ: 25 years of image analysis. *Nat Methods.* 2012, 9(7):671–675.

[45] Püspöki Z, Storath M, Sage D , Unser M. Transforms and Operators for Directional Bioimage Analysis: A Survey. *Adv Anat Embryol Cell Biol.* 2016, 219:69–93.

[46] Forster B, Van De Ville D Fau - Berent J, Berent J Fau - Sage D, Sage D Fau - Unser M , Unser M. Complex wavelets for extended depth-of-field: a new method for the fusion of multichannel microscopy images. *Microsc. Res. Tech.* 2004, 65(1–2):33–42.

[47] Chinga G, Johnsen Po Fau - Dougherty R, Dougherty R Fau - Berli EL, Berli El Fau - Walter J, Walter J. Quantification of the 3D microstructure of SC surfaces. *J. Microsc.* 2007, 227(3):254–265.

[48] Arganda-Carreras I, Kaynig V, Rueden C, Eliceiri KW, Schindelin J, *et al.* Trainable Weka Segmentation: a machine learning tool for microscopy pixel classification. *Bioinformatics.* 2017, 33(15):2424–2426.

[49] Doube M, Kłosowski MM, Arganda-Carreras I, Cordelières FP, Dougherty RP, *et al.* BoneJ: Free and extensible bone image analysis in ImageJ. *Bone.* 2010, 47(6):1076–1079.

[50] Breuls RG, Jiya TU , Smit TH. Scaffold stiffness influences cell behavior: opportunities for skeletal tissue engineering. *Open Orthop J.* 2008, 2:103–109.

[51] Suya H, Fujioka A, Pincelli C, Fukuyama K , Epstein WL. Skin granuloma formation in mice immunosuppressed by cyclosporine. *J Invest Dermatol.* 1988, 90(4):430–433.

[52] Florencio-Silva R, Sasso GR, Sasso-Cerri E, Simões MJ , Cerri PS. Biology of Bone Tissue: Structure, Function, and Factors That Influence Bone Cells. *Biomed Res Int.* 2015, 2015:421746.

[53] Kang ML, Kim HS, You J, Choi YS, Kwon BJ, *et al.* Hydrogel cross-linking-programmed release of nitric oxide regulates source-dependent angiogenic behaviors of human mesenchymal stem cell. *Sci Adv.* 2020, 6(9):5413.

[54] Yu C, Kornmuller A, Brown C, Hoare T, Flynn LE. Decellularized adipose tissue microcarriers as a dynamic culture platform for human adipose-derived stem/stromal cell expansion. *Biomaterials.* 2017, 120:66–80.

[55] Paul A, Manoharan V, Krafft D, Assmann A, Uquillas JA, *et al.* Nanoengineered biomimetic hydrogels for guiding human stem cell osteogenesis in three dimensional microenvironments. *J Mater Chem B Mater Biol Med.* 2016, 4(20):3544–3554.

[56] Marinkovic M, Block TJ, Rakian R, Li Q, Wang E, *et al.* One size does not fit all: developing a cell-specific niche for *in vitro* study of cell behavior. *Matrix Biol.* 2016, 52:426–441.

[57] Lee J, Abdeen AA, Tang X, Saif TA , Kilian KA. Matrix directed adipogenesis and neurogenesis of mesenchymal stem cells derived from adipose tissue and bone marrow. *Acta Biomater.* 2016, 42:46–55.

[58] Kittaka M, Kajiya M, Shiba H, Takewaki M, Takeshita K, *et al.* Clumps of a mesenchymal stromal cell/extracellular matrix complex can be a novel tissue engineering therapy for bone regeneration. *Cytotherapy*. 2015, 17(7):860–873.

[59] Rakian R, Block TJ, Johnson SM, Marinkovic M, Wu J, *et al.* Native extracellular matrix preserves mesenchymal stem cell "stemness" and differentiation potential under serum-free culture conditions. *Stem Cell Res Ther*. 2015, 6:235.

[60] Helms F, Haverich A, Boer U , Wilhelmi M. Transluminal compression increases mechanical stability, stiffness and endothelialization capacity of fibrin-based bioartificial blood vessels. *J Mech Behav Biomed Mater*. 2021, 124:104835.

[61] Maksudov F, Daraei A, Sesha A, Marx KA, Guthold M, *et al.* Strength, deformability and toughness of uncrosslinked fibrin fibers from theoretical reconstruction of stress-strain curves. *Acta Biomater*. 2021, 136:327–342.

[62] Sicchieri LG, Crippa GE, de Oliveira PT, Beloti MM , Rosa AL. Pore size regulates cell and tissue interactions with PLGA-CaP scaffolds used for bone engineering. *J Tissue Eng Regen Med*. 2012, 6(2):155–162.

[63] Li J, Zhi W, Xu T, Shi F, Duan K, *et al.* Ectopic osteogenesis and angiogenesis regulated by porous architecture of hydroxyapatite scaffolds with similar interconnecting structure *in vivo*. *Regen Biomater*. 2016, 3(5):285–297.

[64] Kasten P, Beyen I, Niemeyer P, Luginbühl R, Bohner M, *et al.* Porosity and pore size of beta-tricalcium phosphate scaffold can influence protein production and osteogenic differentiation of human mesenchymal stem cells: an *in vitro* and *in vivo* study. *Acta Biomater*. 2008, 4(6):1904–1915.

[65] Murphy CM, Duffy GP, Schindeler A, O'brien FJ. Effect of collagen-glycosaminoglycan scaffold pore size on matrix mineralization and cellular behavior in different cell types. *J Biomed Mater Res A*. 2016, 104(1):291–304.

[66] Urquia Edreira ER, Hayrapetyan A, Wolke JG, Croes HJ, Klymov A, *et al.* Effect of calcium phosphate ceramic substrate geometry on mesenchymal stromal cell organization and osteogenic differentiation. *Biofabrication*. 2016, 8(2):025006.

[67] Ahn EH, Kim Y, Kshitiz, An SS, Afzal J, *et al.* Spatial control of adult stem cell fate using nanotopographic cues. *Biomaterials*. 2014, 35(8):2401–2410.

[68] García-Gareta E, Coathup MJ , Blunn GW. Osteoinduction of bone grafting materials for bone repair and regeneration. *Bone*. 2015, 81:112–121.

[69] Tan G, Tan Y, Ni G, Lan G, Zhou L, *et al.* Controlled oxidative nanopatterning of microrough titanium surfaces for improving osteogenic activity. *J Mater Sci Mater Med*. 2014, 25(8):1875–1884.

[70] Ibrahim A, Bulstrode NW, Whitaker IS, Eastwood DM, Dunaway D, *et al.* Nanotechnology for Stimulating Osteoprogenitor Differentiation. *Open Orthop J*. 2016, 10:849–861.

[71] Gulseren G, Yasa IC, Ustahuseyin O, Tekin ED, Tekinay AB, *et al.* Alkaline Phosphatase-Mimicking Peptide Nanofibers for Osteogenic Differentiation. *Biomacromolecules*. 2015, 16(7):2198–2208.

[72] Li X, Liu H, Niu X, Yu B, Fan Y, *et al.* The use of carbon nanotubes to induce osteogenic differentiation of human adipose-derived MSCs *in vitro* and ectopic bone formation *in vivo*. *Biomaterials*. 2012, 33(19):4818–4827.

[73] Campi G, Fratini M, Bukreeva I, Ciasca G, Burghammer M, *et al.* Imaging collagen packing dynamics during mineralization of engineered bone tissue. *Acta Biomater*. 2015, 23:309–316.

[74] Auger FA, Gibot L, Lacroix D. The pivotal role of vascularization in tissue engineering. *Annu Rev Biomed Eng*. 2013, 15:177–200.

[75] Tomlinson RE, Silva MJ. Skeletal Blood Flow in Bone Repair and Maintenance. *Bone Res*. 2013, 1(4):311–322.

[76] Nicolaije C, van de Peppel J , van Leeuwen JP. Oxygen-induced transcriptional dynamics in human osteoblasts are most prominent at the onset of mineralization. *J Cell Physiol*. 2013, 228(9):1863–1872.

[77] Zou D, Han W, You S, Ye D, Wang L, *et al.* In vitro study of enhanced osteogenesis induced by HIF-1α-transduced bone marrow stem cells. *Cell Prolif*. 2011, 44(3):234–243.

[78] Zou D, Zhang Z, He J, Zhang K, Ye D, *et al.* Blood vessel formation in the tissue-engineered bone with the constitutively active form of HIF-1α mediated BMSCs. *Biomaterials*. 2012, 33(7):2097–2108.

[79] Zou D, Zhang Z, He J, Zhu S, Wang S, *et al.* Repairing critical-sized calvarial defects with BMSCs modified by a constitutively active form of hypoxia-inducible factor-1α and a phosphate cement scaffold. *Biomaterials*. 2011, 32(36):9707–9718.

[80] Moreno-Jiménez I, Cipitria A, Sánchez-Herrero A, van Tol AF, Roschger A, *et al.* Human and mouse bones physiologically integrate in a humanized mouse model while maintaining species-specific ultrastructure. *Sci Adv*. 2020, 6(44).

[81] Bixel MG, Kusumbe AP, Ramasamy SK, Sivaraj KK, Butz S, *et al.* Flow Dynamics and HSPC Homing in Bone Marrow Microvessels. *Cell Rep*. 2017, 18(7):1804–1816.

[82] Cui H, Zhu W, Nowicki M, Zhou X, Khademhosseini A, *et al.* Hierarchical Fabrication of Engineered Vascularized Bone Biphasic Constructs via Dual 3D Bioprinting: Integrating Regional Bioactive Factors into Architectural Design. *Adv Healthc Mater*. 2016, 5(17):2174–2181.

[83] Wang L, Fan H, Zhang ZY, Lou AJ, Pei GX, *et al.* Osteogenesis and angiogenesis of tissue-engineered bone constructed by prevascularized β-tricalcium phosphate scaffold and mesenchymal stem cells. *Biomaterials*. 2010, 31(36):9452–9461.

[84] Wang MM, Flores RL, Witek L, Torroni A, Ibrahim A, *et al.* Dipyridamole-loaded 3D-printed bioceramic scaffolds stimulate pediatric bone regeneration *in vivo* without disruption of craniofacial growth through facial maturity. *Sci Rep*. 2019, 9(1):18439.

[85] Torroni A, Witek L, Fahliogullari HP, Bortoli JP, Ibrahim A, *et al.* WE43 and WE43-T5 Mg alloys screws tested *in vitro* cellular adhesion and differentiation assay and *in vivo* histomorphologic analysis in an ovine model. *J Biomater Appl*. 2021, 35(8):901–911.

[86] Zhou X, Castro NJ, Zhu W, Cui H, Aliabouzar M, *et al*. Improved Human Bone Marrow Mesenchymal Stem Cell Osteogenesis in 3D Bioprinted Tissue Scaffolds with Low Intensity Pulsed Ultrasound Stimulation. *Sci Rep*. 2016, 6:32876.

[87] Martine LC, Holzapfel BM, McGovern JA, Wagner F, Quent VM, *et al*. Engineering a humanized bone organ model in mice to study bone metastases. *Nat Protoc*. 2017, 12(4):639–663.

[88] Papadimitropoulos A, Scherberich A, Güven S, Theilgaard N, Crooijmans HJ, *et al*. A 3D *in vitro* bone organ model using human progenitor cells. *Eur Cell Mater*. 2011, 21:445–458.

[89] Ramasamy SK, Kusumbe AP, Itkin T, Gur-Cohen S, Lapidot T, *et al*. Regulation of Hematopoiesis and Osteogenesis by Blood Vessel-Derived Signals. *Annu Rev Cell Dev Biol*. 2016, 32:649–675.